Lab on a Chip

PAPER

View Article Online
View Journal | View Issue

Cite this: *Lab Chip*, 2014, **14**, 1357

Direct measurement of the differential pressure during drop formation in a co-flow microfluidic device†

Ke Xu,‡ Chris P. Tostado,‡ Jian-Hong Xu,* Yang-Cheng Lu and Guang-Sheng Luo*

Received 30th October 2013,
Accepted 20th January 2014

DOI: 10.1039/c3lc51222c

www.rsc.org/loc

In this study, we developed a new method for the direct measurement of differential pressures in a co-flow junction microfluidic device using a Capillary Laplace Gauge (CLG). The CLG – used inside the microchannel device – was designed using a tapered glass-capillary set up in co-flow junction architecture with a three-phase liquid–liquid–gas system with two flowing liquid phases and an entrained gas phase. By taking advantage of the Laplace equation, basic geometric relations and an integrated image analysis program, the movement of the entrained gas phase with the flow of the liquid-phases is tracked and monitored, allowing the gauge to function as an ultra-sensitive, integrated, differential pressure sensor measuring fluctuations in the liquid-dispersed phase channel pressure as small as tens of Pascals caused by droplet formation. The gauge was used to monitor the drop formation and breakup process in a co-flow junction microfluidic device under different flow conditions across a large range (1×10^{-3} to 2.0×10^{-1}) of capillary numbers. In addition to being able to monitor short and long term dispersed phase pressure fluctuation trends for both single drop and large droplet populations, the gauge was also used to clearly identify a transition between the dripping and jetting flow regimes. Overall, the combination of a unique, integrated image analysis program with this new type of sensor serves as a powerful tool with great potential for a variety of different research and industrial applications requiring sensitive microchannel pressure measurements.

Introduction

Over the past several years, the use of microfluidic techniques for the execution of chemical processes,[1] for the production of novel materials,[2] and in various analytical devices[3,4] has become quite common and mainstream due to the repeatedly proven reliability of these techniques and the often simple and elegant designs of the microfluidic devices themselves. Furthermore, microfluidic phenomena, and in particular, the breakup process of multi-phase emulsions which is paramount for understanding and successfully applying these techniques for various purposes, have been studied at length.[5–8] Recently, the use of new microfluidic designs and devices as analytical tools for characterizing the essential properties of multi-phase systems and flow within various microchannel geometries has also become more common. Microfluidic devices have been designed specifically to characterize important properties of multiphase systems such as the interfacial tension[9] and the viscosity,[10,11] both of which are essential for determining emulsion formation, emulsion stability and flow regimes within microchannels. Several interesting designs have also been developed for the specific purpose of closely studying relevant phenomena (such as droplet breakup) observed in microfluidic systems. The production of monodispersed droplets is one of the most ubiquitous and widely used techniques in microfluidics specifically because of its versatility and the fidelity with which the technique can be replicated. Thus, the conditions under which monodispersed liquid–liquid emulsions – usually an organic liquid dispersed phase in an aqueous continuous phase (O/W) or *vice versa* (W/O) – can form have been closely studied. In microfluidics, the capillary number, $Ca = u_m\mu/\gamma$ (where μ is the viscosity of the continuous phase, u_m is the velocity of the continuous phase, and γ is the liquid–liquid interfacial tension) is a commonly used non-dimensional number relating the system's viscous shear force to the interfacial force. The Ca number thus serves as both 1) an important measure of the balance between shear and interfacial forces and 2) a qualified indicator of the type and nature of the emulsion formed because it is precisely this balance which dictates the expected flow regime.[5]

The State Key Lab of Chemical Engineering, Department of Chemical Engineering, Tsinghua University, Beijing 100084, China. E-mail: xujianhong@tsinghua.edu.cn, gsluo@tsinghua.edu.cn; Fax: +86 10 62773017; Tel: +86 10 62773017

† Electronic supplementary information (ESI) available. See DOI: 10.1039/c3lc51222c

‡ These authors contributed equally to this work.

The interplay between interfacial and viscous forces within the microfluidic channel determines the manner of droplet breakup. At high Ca numbers (~1.0×10^{-2} to 1.0×10^{-1}) when the viscous forces are relatively strong compared to the interfacial forces, the viscous shearing force of the continuous phase on the dispersed phase strongly influences drop size. However, at low Ca numbers (~1×10^{-4} to 1×10^{-3}) interfacial forces are relatively strong compared to the viscous shear, and partial blockage of the microfluidic channel by the dispersed phase can occur. Thus, one of the most important characteristics of multiphase systems for studying droplet breakup – especially in the lower Ca number range – is the channel pressure and in particular, the differential pressures between phases. Recently, several studies have focused on pressure measurements within microfluidic channels for the specific purpose of studying droplet breakup and multi-phase flow.[12–15] Our previous work also focused on developing a pressure drop measurement system in which we combined standard industrial-use differential pressure sensors with a specialized circuit containing several signal amplifiers to detect droplet dispersion induced pressure fluctuations in a T-junction microchannel.[15]

The vast majority of these microfluidic tools depends strongly on the actual physical architecture of the channel itself. The material used for the device (which influences wetting), the size of the channel, and the placement of the sensor can all dramatically affect the channel pressure especially considering the sensitivity required for the measurements. In addition, a common characteristic of most of these studies is that they have thus far focused on T-junction architectures as they are well characterized and are one of the most familiar and widely used types of microfluidic devices in the literature. However, in this study, we focus on measuring the pressure within a co-flow junction microfluidic device – another widely used architecture with unique advantages: a radial axis of symmetry ensuring uniform viscous shearing, a more limited potential for dispersed phase wetting, and a quick and easy modular device construction. Measuring the pressure within co-flow junction channels presents an opportunity to compare pressure measurements among different channel architectures as well as investigate new phenomenon, such as dynamic interfacial tension, in a way in which they could not be examined (in wetting-prone designs) otherwise.

Yet another integral part of developing tools for channel pressure measurements involves visual analysis. Pressure fluctuations and patterns are associated with the drop cycle as the drop grows and is eventually squeezed or sheared off; hence, synchronization between the different phases of drop growth and channel pressure measurements can be a challenge. Visual analysis is performed using CCD cameras coupled with a microscope to capture the multi-phase flow and record a video of the droplet breakup process. Often, pressure measurements are recorded separately from this process and must be synchronized to compare the different stages of drop formation and their associated pressure fluctuations. Our recent study required the inclusion of an electronic switch to synchronize the capture of images with the beginning of differential pressure signal acquisition to ensure that pressure signals did in fact correspond to the appropriate stage of drop growth.

Thus far, very few studies have focused on developing methods for channel pressure measurements integrated into the basic design of the microfluidic device and even fewer have proposed simple, easily replicated methods. Recently, however, Abate *et al.* developed a new integrated T-junction microchannel pressure sensing device aptly named "Laplace Sensor" due to its utilization of the balance between interfacial tension, interfacial radial curvature, and the pressure differential across the interface as described by the Laplace law:[13]

$$\Delta P = \gamma\left(\frac{1}{R_1} + \frac{1}{R_2}\right), \quad (1)$$

where ΔP is simply referred to as the Laplace pressure or P_{Laplace}. The pressure gauge developed here is integrated directly into the co-flow microchannel design itself and similarly uses the Laplace law to derive differential pressure measurements albeit in a totally unique manner. Here, we have combined the use of an immobile gas phase to measure the pressure differential of a two phase liquid–liquid system. Thus, in this study, by applying the principles of the Laplace law, we developed a new microfluidic tool for the direct measurement of the differential pressure of the dispersed phase in a liquid–liquid two phase co-flow junction microfluidic device. Using this tool, along with our unique method of visual analysis which combines drop formation monitoring and pressure measurement into a single seamless process, we examined the differential pressure fluctuations for different systems with various interfacial tensions under various conditions and flow rates across a large range of capillary number values.

Materials and methods

Co-flow microchannel, CLG, materials and instruments

Co-flow microchannels and similar co-flow junction geometries have been utilized quite extensively by researchers in the field of microfluidics to study important fundamental scientific topics such as dynamic interfacial tension and the formation of monodispersed and complex drop populations and to explore novel methods for the fabrication of functional materials.[16–22] However, no simple and reliable method for the detection of the inner channel pressure has been developed, thereby limiting the scope to which this co-flow junction's structure may be applied. Herein, we choose such a microchannel structure as an example to show that the CLG could be used in structures where traditional sensors are typically unavailable.

Polymethyl methacrylate (PMMA) was used to fabricate the scaffold of the co-flow microfluidic device, and borosilicate glass capillaries were used as channels. The inner diameter of

the outer capillary channel was 1050 μm. The outer diameter of the tip of the tapered-end of the middle capillary was approximately 100 μm, and this capillary was inserted coaxially into the outer capillary channel. Tapered capillary tips were fabricated using a micropipette puller (P-97, SUTTER Co. Ltd., USA). The flow rates of the two liquid phases were controlled using four syringe pumps and four gastight syringes (LSP01-1B, Baoding Longer Precision Pump Co., Ltd).

The CLG, a tapered glass capillary which contained the entrained gas phase, was placed inside the middle capillary such that the tapered ends of the two capillaries were nearly flush with one another. The inner diameter of this gas capillary was 500 μm, whereas the tip was tapered to approximately 10 μm. Another gastight syringe was used for the storage of gas, the volume of which was much larger than the channel volume in order to ensure constant pressure. In order to simplify the calculation by assuming complete wetting of the innermost capillary channel by the aqueous phase, we first wet the inner wall of the gas capillary using 20% NaOH aqueous solution for several hours followed by washing with pure water before beginning flow experiments.

The experimental setup as well as an image of a typical device used for experiments are shown in Fig. 1(a–c).

From Fig. 1 it may be noted that the CLG (innermost capillary) is slightly misaligned with the dispersed phase capillary (middle capillary). We thus performed an experiment to determine the influence of both the presence of CLG in the setup and the position (alignment) of the CLG on the measurement data. The results (shown in the ESI,† Fig. S3) show that under the same flow conditions, neither the presence nor the placement of the CLG within the inner capillary affects the final drop size, and the results obtained from CLG at different placements are similar. This slight misalignment therefore has no effect on the pressure measurement capability of the CLG.

It should also be pointed out that the combination of the CLG sensor and the microchannel is not permanent. A CLG fixed in one place could be moved to another place if necessary, and if a CLG device were to fail, it could be easily replaced by a new one without destroying the microchannel – an advantageous design characteristic of this type of sensor.

In this work, we designated pure distilled water (dispersed phase) and pure octanol (continuous phase) as a standard system to study the pressure gauge and used 5 wt% Tween 80 aqueous solution in other experiments to examine a wider range of interfacial tension values. *N*-Octyl alcohol and Tween 20 were purchased from J&K Scientific Ltd. All of the experimental videos and images were taken using an optical microscope (BX61, Olympus, Japan) equipped with a high-speed camera, with a frequency of up to 10 000 images per second (DK-2740, Dantech, Denmark).

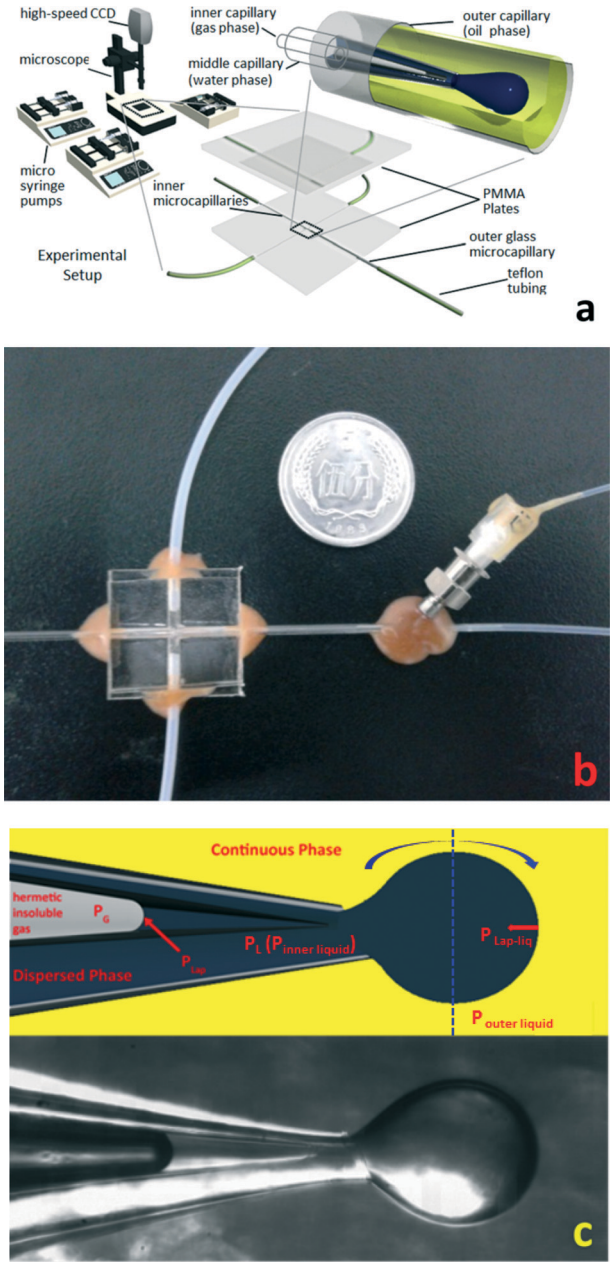

Fig. 1 (a) The schematic images of CLG and the whole platform. (b) Real channel fabricated and used for this experiment. (c) The detail of the capillary tip and the CLG, as well as the forces and pressures.

The mathematical model of the CLG

One key problem in designing a dynamic local pressure gauge in microchannels is the considerable perturbation of the flow generated by the sensor/gauge itself, and eliminating this unwanted side-effect is key to any successful device. An additional challenge results from the need to synchronize the pressure measurements with the instantaneous flow conditions in the channel or at the junction. This characteristic is especially important and necessary when studying dynamic processes requiring fast, accurate, and localized measurements, such as the formation and breakup of droplets in an emulsion. In order to satisfy both of these requirements, we introduced a microcapillary into the system containing an insoluble, entrained gas phase connected to a relatively large hermetic gas storage chamber. At a specific gas pressure,

liquid will flow into the gas capillary until a force balance on the gas–liquid interface is established (Fig. 1(c)):

$$P_L = P_G - P_{Lap} \quad (2)$$

where P_L is the local pressure of the liquid phase, P_G is the pressure of the gas phase, and P_{Lap} is the capillary force brought about from the gas–liquid interface. Since P_G is measured directly from the gas storage container, the local liquid pressure, P_L, can be easily calculated if P_{Lap} is known.

By observing the interface between the liquid and gas phases, P_{Lap} in a tapered capillary can be calculated using the Laplace equation:

$$P_{Lap} = \frac{2\gamma_{L-G}}{r} \quad (3)$$

where γ_{L-G} is the interfacial tension between the gas and the liquid, and r is the radius of curvature of the interface. Prior studies have calculated P_{Lap} by directly analyzing and identifying the location of the interface boundary in the image and then computing the curve radius according to that estimation.[13] However, this simple method is limited by the quality and size of the image taken as well as the ability of the image analysis algorithm to detect the location of the changing interface. The algorithms often rely on fitting a circle or an ellipse to the boundary interface based on a measurement of several points along the interface. Because of the pixel size and refraction of the round channel walls, such a fitting method can introduce an error affecting the sensitivity of the device.

Here, we demonstrate a different, more accurate method for calculating P_{Lap} without having to directly measure the entire two-phase interface. As shown in Fig. 2, we can derive the following relationship between the curve radius and other parameters:

$$\frac{1}{r} = \frac{\tan\left(\frac{\pi}{4} - \frac{\theta+\varphi}{2}\right)\cdot\left(1+\frac{\sin\theta}{\cos\varphi}\right)}{l\tan\varphi} \quad (4)$$

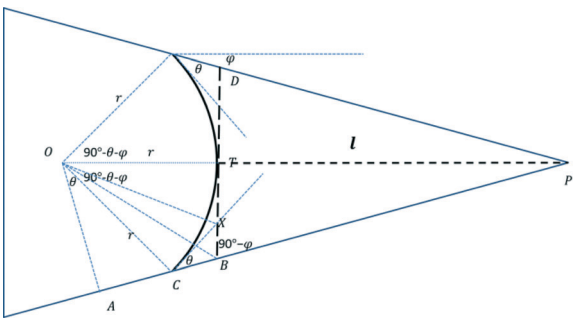

Fig. 2 A schematic expressing the detection of the curve radius, r, using easily-detected parameters. The taper represents the inner wall of the gas capillary. O is the centre of the interface sphere, OA is perpendicular to the wall, and line BT is tangent to the interface sphere at T where T is the right top of the interface. P is the top angle of the taper, and l is the length of PT.

A detailed derivation is provided in the ESI. In this equation, l is the distance between the tapered tip P and the tangent line to the center of the interface, θ is the angle between the interface and the wall, and φ is the angle between the wall and the horizontal line. Combining this with the Laplace equation, we get:

$$P_{Lap} = \frac{2\gamma_{L-G}}{r} = 2\tan\left(\frac{\pi}{4} - \frac{\theta+\varphi}{2}\right)\cdot\left(1+\frac{\sin\theta}{\cos\varphi}\right)\cdot\frac{\gamma_{L-G}}{l\tan\varphi} \quad (5)$$

However, the triphase-contact-angle is still hard to measure. In order to address this and simplify the model, we wet the inner wall of the gas capillary with the liquid phase to eliminate the triphase interface, thereby equating $\theta = 0$. The equation is then simplified to:

$$P_{Lap} = \frac{2(1-\sin\varphi)}{\sin\varphi}\cdot\frac{\gamma_{L-G}}{l} \quad (6)$$

In this image analysis process, l and φ are much easier and more accurate to compute than r. For example, in these experiments, the curve radius of the gas–liquid interface was approximately 20 μm, while the pixel size was 1.81 μm. Thus, the error brought about by a single pixel difference in measurements would be approximately 10%. At the same time, typical l values were greater than 300 μm, resulting in a much lower pixel error. Furthermore, distortion due to refraction is more prominent in the radial dimension than in the axial dimension in a round capillary; measuring r would require a clear visual of the interface near the capillary wall where distortion is greatest, whereas measuring l would involve a measurement along the center of the capillary where distortion is minimal. By applying eqn (6), we can calculate P_{Lap} more easily and accurately. If the gas capillary is appropriately tapered, φ could be treated as a constant (refer to ESI†), and by simply gauging the variation of l, we can obtain the fluctuation in P_{Lap}. In such a case, the interface will move forward and backward along the taper in accordance with the fluctuation of the local pressure.

Here, three assumptions are necessary for the above equation to be applicable. First, we assume that the interface between the gas and the liquid is spherical. Second, the inner wall of the gas capillary is completely wetted by the aqueous liquid phase such that the spherical interface is tangent to the inner wall. Third, a volume change in the CLG does not affect the flow rate of the dispersed phase. Furthermore, if the gas pressure is constant, we can derive:

$$P_L = P_G - \frac{2(1-\sin\varphi)}{\sin\varphi}\cdot\frac{\gamma_{L-G}}{l} \quad (7)$$

relating the local liquid pressure with the easily measured parameters: l and φ. In this work, P_L is also designated as $P_{\text{inner liquid}}$ to emphasize the difference between the

pressures associated with the inner aqueous liquid phase and the outer organic liquid phase.

Image analysis

Image processing was performed using a MATLAB program designed with a simple graphical user interface (GUI). AVI videos produced from the microchannel flow experiments were imported into the program and each frame of the video was enumerated and analyzed sequentially. Before any experiments were conducted and immediately following the fabrication of the microfluidic device, the physical boundaries of the microcapillary pressure gauge within the microchannel and the angle between these boundaries, φ, were measured using a microscopic image of the CLG device and the Image Tool imaging software. These measured boundaries were then used by the GUI to automatically calculate a central line along which gas bubble movement was to be detected. These measured physical boundaries and the accompanying calculated center line were specific to each CLG device and do not change (Fig. 3b). After these boundaries have been set in the GUI, the MATLAB program can continue with image analysis. However, prior to the actual image analysis, the program executes several pre-image analysis steps to prepare each image for optimal analysis; before each image in the video is analyzed, it is 1) converted to a grayscale image with the 2) contrast adjusted accordingly, 3) cropped, 4) converted to a black and white image and 5) filtered to remove errant, non-essential pixels. The image is then ready to proceed with analysis. At this point, the program determines the position of the tip of the bubble along the axis by identifying the boundary between black and white pixels along the calculated center line. The program also determines the inner diameter of the microcapillary pressure gauge at that point and the distance of the gas–liquid interface from the interpolated CLG tip. This information together with several simple trigonometric relations allow for the calculation of the bubble's spherical cap's radius of curvature and combined with the Laplace equation can be used to accurately determine the differential pressure difference of the dispersed phase. For each particular experiment under different flow conditions, at least 500 images were analyzed to adequately determine pressure trends with each image requiring only a fraction of a second for analysis using a commercial laptop with an Intel i7 processor with an integrated video card and 8 Gb of RAM.

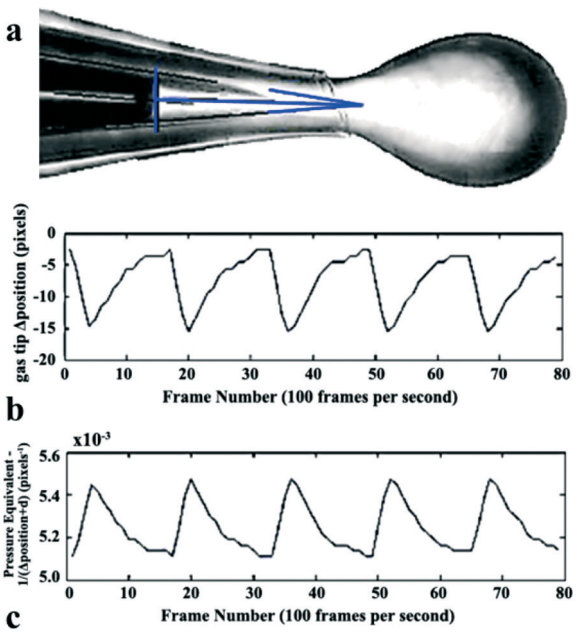

Fig. 3 Image capture of the image analysis program used to identify and track the movement of the gas phase within the inner glass capillary. a) Typical image with auxiliary (blue) lines. b) Graph of the distance between the gas phase tip and the right tip of the CLG (l in eqn (6)) in pixels. c) Differential pressure equivalent ($1/l$ in eqn (6)) in pixels^{-1}.

Results and discussion

Verification of assumptions

Before further analysis, we must first verify the assumptions mentioned above to support the physical and mathematical model proposed.

First, by pumping an aqueous phase solution of 20 wt% NaOH through the inner gas capillary for a period of 2 hours with the goal of covering the glass surface with a thin, highly hydrophilic film completely saturated with water, we ensure the complete wetting of the inner wall of the gas capillary by the aqueous phase. In this case, the gas phase does not directly contact with the inner wall of the capillary, and the liquid–gas interface should fit a spherical cap model. The interface between the dispersed phase and the gas phase was subsequently measured using the DataPhysics OCA20 tensiometer software to validate that the interface was indeed spherical (data not shown). Thus, by eliminating the triphase interface, the gas–liquid interface can be assumed to be tangent to the inner glass wall, as seen in Fig. 4(a).

The effect of flow inside the CLG on the dispersed phase liquid flow was also examined. In the experiment shown in Fig. 4, the volume displaced with the forward and backward motion of the liquid–gas interface throughout the droplet dispersion process is approximately 2.0×10^{-4} μl, while the drop's volume (~500 μm in diameter) is 0.065 μl. The ratio of these two volumes is less than 0.3%, which is smaller than the error of the pump (0.5%) used in the experiment itself. Thus, we can assume that the backward/forward motion of the gas–liquid interface has a negligible effect on the flow outside the CLG tip.

Next, we check our assumption regarding constant gas pressure. As mentioned before, the volume displaced with the forward and backward motion of the gas phase head with the dispersion of droplets is on the scale of 10^{-4} μl. Conversely, the volume of the gas storage chamber used in these experiments was greater than 10 ml with a constant temperature and a gas pressure set slightly above 10^5 Pa (barometric pressure). According to the Ideal Gas State Equation $PV = nRT$,

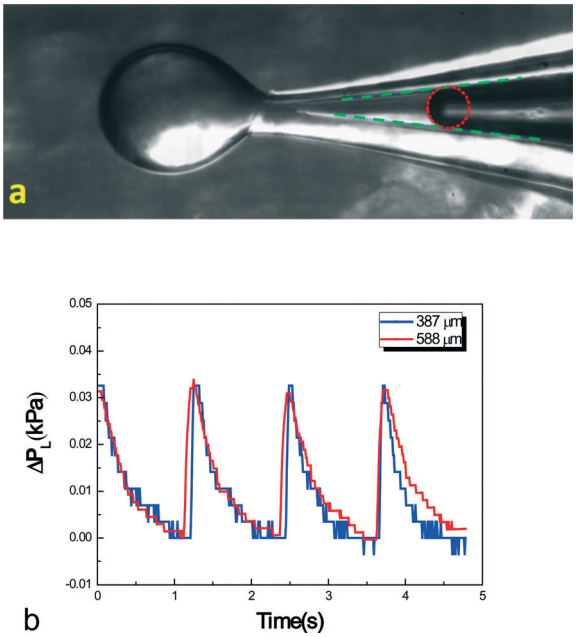

Fig. 4 Verification of assumptions for the physical and mathematical models. (a) The red circle matches the gas–liquid interface perfectly, and the tangent to the inner wall of the gas capillary is represented as blue lines. (b) A comparison of the differential pressure signal measured when the interface is at l = 387 μm and l = 588 μm, showing the error of inner resistance. Note: ΔP_L is defined as $\Delta P_L = P_L - P_{L(origin)}$, where $P_{L(origin)}$ is the inner liquid pressure measured using eqn (6) and (7) at the original position of the gas phase tip in the first frame recorded in the data. As always, we choose a frame close to the minimum value of P_L over a drop cycle as the first frame.

where P is the gas pressure, V is the gas volume, R is the gas constant and T is the gas temperature, the pressure fluctuations resulting from these changes in volume were on the order of 10^{-2} Pa, much smaller than the Laplace pressures measured in our experiments which ranged from 10 to 100 Pa. Therefore, we can also neglect these volume-associated changes in pressure and assume that the gas pressure is constant.

Error analysis

Before utilizing any new device, it is essential to thoroughly evaluate its error. For this CLG, there are several possibilities for the introduction of error into the final differential pressure calculation.

First, we consider the resolution, or the error in the Laplace pressure calculation brought about by the pixel size of the image. In the following experiments, the pixel size (δl) is 1.81 μm. In this case, the error caused by pixel size (δP_{Lap}, different from ΔP_{Lap} defined previously) can be calculated as:

$$\delta P_{Lap} = \frac{2(1-\sin\varphi)\gamma_{L-G}}{\sin\varphi}\cdot\delta\left(\frac{1}{l}\right) \approx \frac{2(\sin\varphi-1)\gamma_{L-G}}{\sin\varphi}\cdot\frac{\delta l}{l^2} \quad (8)$$

In these experiments, Δl (the range of movement of the gas–liquid interface) was approximately 50 μm, and l was typically >350 μm. Thus, we can calculate the error of the Laplace pressure relative to the differential Laplace pressure and the actual Laplace pressure:

$$\left|\frac{\delta P_{Lap}}{\Delta P_{Lap}}\right| \approx \left|\frac{\delta l}{\Delta l}\right| = \left|\frac{1.81}{50}\right| = 3.6\% \quad (9)$$

$$\left|\frac{\delta P_{Lap}}{P_{Lap}}\right| \approx \left|\frac{\delta l}{l}\right| < \left|\frac{1.81}{380}\right| = 0.5\% \quad (10)$$

The error associated with pixel size can be limited (*e.g.* <5%) by changing the design of the CLG taper (and the initial position of gas–liquid interface) to accommodate different systems. A longer taper would result in a smaller φ value and therefore a larger Δl. Utilizing a microscope with a higher pixel resolution (resulting in a smaller δl) can also reduce such an error.

The error associated with the resistance of the dispersed liquid phase inside the CLG was also considered. Using octanol as the continuous phase and air-saturated 5 wt% Tween 80 aqueous solution as the dispersed phase, we conducted two drop dispersion experiments by setting the dispersed and continuous phase flow rates to 400 μl min^{-1} and 2 μl min^{-1}, respectively, while varying the starting position of the gas–liquid interface in the CLG by adjusting the pressure of the gas reservoir, thereby setting the initial value of l (Fig. 2). Here, l (the distance between the center of the gas–liquid interface and the interpolated apex) was set to 387 μm and 588 μm, and the differential pressure measurement results are shown in Fig. 4(b). The two curves generated from different gas–liquid interface starting positions indeed have a similar shape. Although the 588 μm curve has a slightly shorter peak – which might be caused by a slight increase in the flow resistance of the liquid inside the CLG – the average difference in peak height is less than 1.5 Pa – relatively small compared to the final measurement results (~30–100 Pa). All subsequent differential pressure measurement experiments in this study were conducted such that the gas–liquid interface was always located in the range 387 μm ≤ l ≤ 588 μm. Thus, the pressure measurements taken using the CLG were largely independent of the initial position of the gas–liquid interface.

The resistance associated with the positioning of the gas–liquid interface inside the CLG can change, however, depending on several different parameters. Increasing the diameter of the CLG tapered tip (the gas capillary tip) or moving the gas–liquid interface position forward would both result in a lower resistance. Conversely, if the drop frequency is too high (Ca > 0.26), or the pressure fluctuation is extremely low, the resistance can increase and should be taken into consideration as the resulting error will be more significant.

The influence of φ on the final differential pressure measurements was also evaluated. φ is a system parameter of the device, set during fabrication of the capillary taper. φ was determined using a microscope and Image Tool software to

measure the angle and did not change during the image analysis process. From eqn (6), we can obtain:

$$\frac{\partial P_{\mathrm{Lap}}}{\partial \varphi} = -\frac{2\gamma_{\mathrm{D-G}}\cos\varphi}{l\sin^2\varphi} \tag{11}$$

After rearrangement of the above equation, we have:

$$\frac{\dfrac{\mathrm{d}P_{\mathrm{Lap}}}{P_{\mathrm{Lap}}}}{\dfrac{\mathrm{d}\varphi}{\varphi}} = -\frac{\varphi\cos\varphi}{(1-\sin\varphi)\sin\varphi} \to -1, \tag{12}$$

showing that every 1% error in φ results in a corresponding differential pressure measurement error of 1%. Thus, to ensure accuracy for each CLG device, φ was measured numerous times, and an average angle was used for all subsequent analysis.

Setting ΔP_{Lap} = 50 Pa, and assuming an inner resistance of 1.5 Pa and a 1% error in φ as a typical case, we can estimate the total error propagation from the final differential pressure measurements:

$$\frac{\delta P_{\mathrm{Lap}}}{\Delta P_{\mathrm{Lap}}} = \sqrt{\left(\frac{1.81}{50}\right)^2 + \left(\frac{1.5}{50}\right)^2 + \left(\frac{1\%}{100\%}\right)^2} \times 100\% = 4.8\% \tag{13}$$

The typical propagated error associated with the CLG is ~5%. Although there are several different aspects of the CLG measurement method in which error may be introduced, the overall effect of the combined error on final differential pressure measurements is not very large. Furthermore, small changes to the CLG device parameters (*i.e.* smaller φ, larger CLG tip diameter, smaller pixel size) can result in increased accuracy. Moving the initial position of the gas–liquid interface backward can reduce the error associated with pixel size but may increase the error caused by resistance inside the CLG. So, depending on the acceptable amount of error caused by resistance, the interface position should be adjusted to each system accordingly. In this work, the focus was on verifying the validity and use of the CLG device. More precise and accurate CLG devices will be designed and applied in future work.

Single drop analysis and drop breakup mechanism

One of the key aspects of understanding dynamic flow and droplet breakup in microchannels involves investigating the interplay between interfacial (pressure-driven) and viscous (shear-driven) forces.[5] Fig. 5(a–e) shows an analysis of a complete drop cycle including the relationship between channel blockage and differential pressure. In this section, the diameter of the dispersed phase tip is 72 μm. For single drop analysis, distilled water was used as the dispersed phase while octanol was used as the continuous phase with the dispersed and

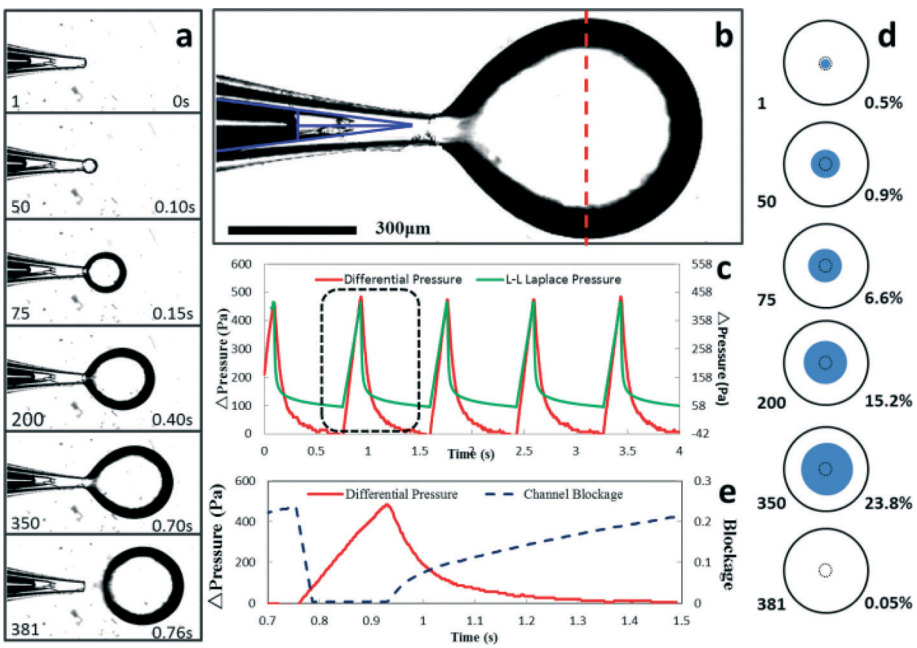

Fig. 5 The breakup process of a single drop in the co-flow junction microchannel. a) Sequential images of the growing drop and breakup captured at 0.73 s, 0.83 s, 0.88 s, 1.13 s, 1.43 s and 1.49 s, respectively. b) A typical image used for image analysis with superimposed boundary lines, a center line and an interface analysis line. The dotted lines signify the region of interest when considering the differential pressure of the continuous phase, $\Delta P_{\mathrm{outer\ liquid}}$, on the drop's surface. c) A comparison between the measured dispersed phase and the liquid–liquid Laplace differential pressures calculated from the droplets' diameter. Note: the left *Y*-axis is for the red curve and the right *Y*-axis is for the green one. d) The relationship between differential pressure and channel blockage for an entire drop cycle. e) Cross-sectional view of the capillary channel showing channel blockage corresponding to the sequential images shown in (a).

continuous flow rates set at 6 μl min^{-1} and 600 μl min^{-1}, respectively. The video capture rate was 500 fps and flow conditions were allowed to reach a steady state before recording began. 2000 images were analyzed using the MATLAB GUI. This sequence of images covers more than 4 complete drop cycles including breakup. Fig. 5(a) shows images of the droplet breakup process over a period of 4 seconds. The differential pressure over this period was recorded using the same image analysis process described earlier (Fig. 5b). To examine the relationship between channel blockage and dispersed phase differential pressure, the images were analyzed again using a separate MATLAB program to calculate the drop diameter. A direct comparison of the dispersed phase differential pressure (in differential pressure equivalent units calculated directly by the MATLAB program) and channel blockage is shown in Fig. 5(e). The channel blockage, defined as the percentage of the capillary channel cross-sectional area occupied by the growing drop, is shown in Fig. 5(e).

The dispersed phase differential pressure decreases steadily as the size of the growing droplet increases, reaching a minimum right before drop breakup. Differential pressure spikes immediately following drop breakup and then continues to slowly decrease with the next cycle. Channel blockage expectedly follows an opposite trend with a maximum channel blockage (23.8%) occurring immediately before breakup.

In order to relate our experimental data to a physical model, we perform a pressure balance analysis beginning with the definition of the Laplace pressure (eqn (1)) at a given cross-section of the drop (in this case, the center of the growing drop denoted by the dashed line shown in Fig. 5b):

$$P_{\text{inner liquid}} = P_{\text{Lap–liq}} + P_{\text{outer liquid}} \quad (14)$$

As we are more concerned with pressure fluctuations (differential pressures) than the absolute values of the pressures themselves, we designate a standard reference pressure, $P_{\text{inner liquid(origin)}}$, which, in this case, is the lowest inner-liquid pressure in a drop cycle. We can then rewrite eqn (14) as:

$$\Delta P_{\text{inner liquid}} = \Delta P_{\text{Lap–liq}} + P_{\text{outer liquid}} \quad (15)$$

where $\Delta P_{\text{inner liquid}}$ is defined as $P_{\text{inner liquid}} - P_{\text{inner liquid(origin)}}$, and $\Delta P_{\text{Lap–liq}}$ is defined as $P_{\text{Lap–liq}} - P_{\text{inner liquid(origin)}}$.

In Fig. 5(c), we show a comparison between $\Delta P_{\text{inner liquid}}$, which is directly measured using the CLG, and $\Delta P_{\text{Lap–liq}}$, which is calculated by measuring the changing shape of the droplet as it grows, following its definition from eqn (1):

$$P_{\text{Lap–liq}} = \gamma\left(\frac{1}{R_1} + \frac{1}{R_2}\right), \quad (16)$$

where R_1 and R_2 are the primary and secondary radii of curvature.

We then find that we can divide the drop growth progress into two distinct stages: an initial growth stage and a terminal growth stage. In the first stage, from 0 to approximately 0.1 s of the droplet growth cycle, $\Delta P_{\text{inner liquid}}$ and $\Delta P_{\text{Lap–liq}}$ exhibit similar change, with both values decreasing rapidly. Therefore, according to eqn (15), $P_{\text{outer liquid}}$ must be approximately constant. This makes physical sense as during the early stages of droplet growth, the droplet is most likely too small to significantly affect the continuous phase flow field. In this case, the inner liquid differential pressure changes according to the changes in the liquid–liquid Laplace pressure.

After that short period of approximately 0.1 s, the two differential pressures begin to diverge with $\Delta P_{\text{inner liquid}}$ continuously decreasing while $\Delta P_{\text{Lap–liq}}$ stays relatively constant. We hypothesize that the difference between these two differential pressures is due to the drop size having grown large enough to begin to affect the continuous phase flow field around it. Assuming a constant volumetric flow rate of the continuous phase, the growing droplet restricts the passway of the continuous phase, increasing the velocity of the outer liquid through the section, which, according to Bernoulli's equation, can significantly decrease the outer liquid pressure, $P_{\text{outer liquid}}$. This phenomenon is particularly significant as significant fluctuations in $P_{\text{outer liquid}}$ can, in addition to shear, potentially create a "plugging–squeezing" effect in which differences between the upstream and downstream channel pressures create an additional driving force for droplet breakup in co-flow junction microchannels (similar to that observed previously in T-junction channels). The extent to which the continuous phase influences the drop growth and breakup process in a co-flow junction microchannel still requires further verification however (direct measurement of the outer liquid pressure) and is outside the scope of this initial work but will be the focus of future research.

Dependence on the capillary number

In this initial study, the CLG was used to monitor changes in differential dispersed phase pressures across a wide range of Ca numbers. In the following two sections, the diameter of the dispersed phase tip is 130 μm. Here, we chose octanol as the continuous phase and 5 wt% Tween 80 aqueous solution as the dispersed phase. The dispersed phase flow rate was fixed at 6 μl min^{-1} while the continuous phase flow rate varied from 20 μl min^{-1} to 4000 μl min^{-1}, with Ca numbers ranging from 0.001 to 0.26, respectively. From Fig. 6 we can observe that the frequency of droplet formation increases with Ca while the phase length and amplitude of the differential pressure signals both decrease. Using a video capture rate of 100 fps and a resolution such that one pixel = 1.81 μm,[2] we could identify distinct pressure peaks for Ca numbers as high as 0.26 (Fig. 6, inset). We assume that using a higher microscopic magnification coupled with a faster CCD capture rate would allow us to identify peaks with greater drop frequency and weaker pressure fluctuations.

The Ca number associated trends mentioned above agree with the results of another prior study[16] on co-axial capillary microfluidic devices. In that study, the authors specifically

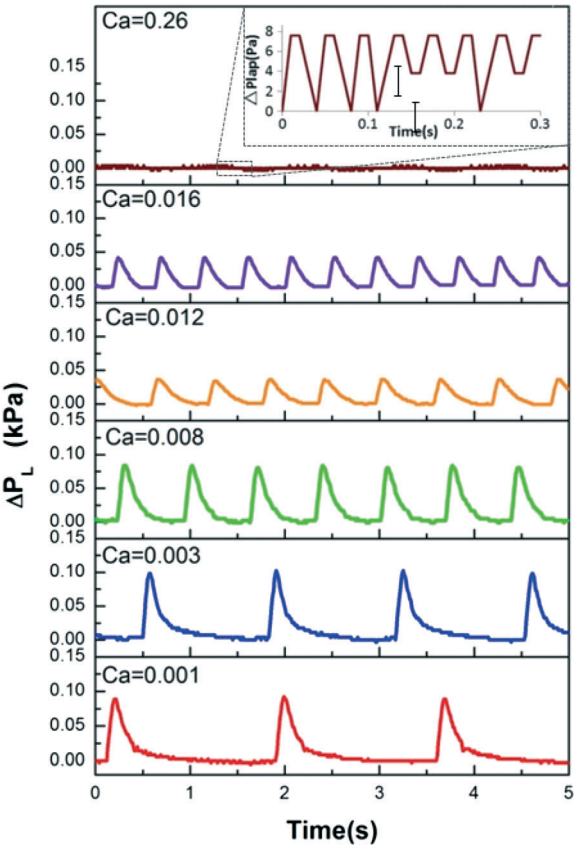

Fig. 6 Pressure fluctuations measured by CLG with a fixed dispersed phase (5% Tween 80 in water) flow rate of 6 μl min^{-1} and a variable continuous phase (pure octanol) flow rate ranging from 20 μl min^{-1} to 4000 μm min^{-1}, with the Ca number ranging from 0.001 to 0.26, respectively.

discussed the different flow regimes (*i.e.* dripping flow and jetting flow) produced in the microfluidic devices with respect to the We number of the dispersed phase and the Ca number of the continuous phase. The flow regimes observed in our experiments match the data shown in that study, supporting the validity of our experimental results in terms of these dimensionless variables. Our results also share a similar trend to those presented in studies on microchannel pressure measurements made in T-junction microdevices[13] regarding the pressure peaks becoming weaker and more frequent with the increase of Ca.

Pressure fluctuations from dripping flow to jetting flow

According to prior studies[23] conducted using co-axial microfluidic devices, the inertial forces of the inner fluid are balanced by the surface tension forces. For a given continuous phase Ca value, this balance is given by the inner Weber number, $We_{in} = \rho_{in} d_{tip} u^2_{in}/\gamma$, where ρ_{in} is the density of the inner phase, u_{in} is the average flow rate, and γ is the interfacial tension between the inner dispersed phase and the continuous phase. When We is small, surface tension dominates, and the system produces monodispersed drops. As We increases, the dripping frequency also increases. When We ≥ O(1), the

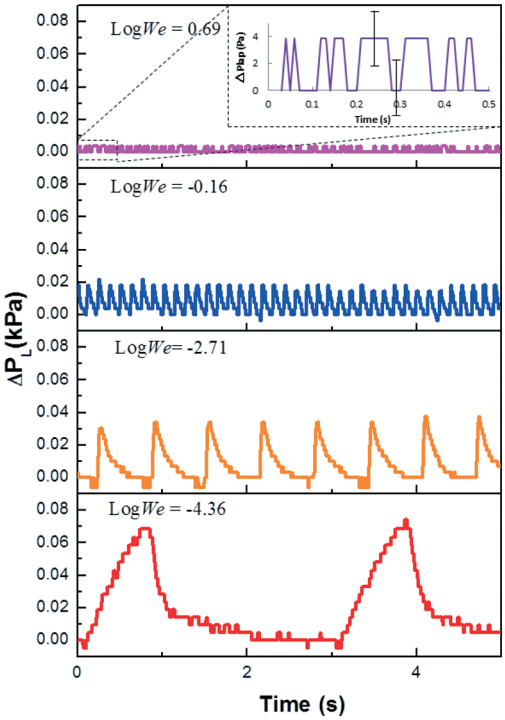

Fig. 7 Pressure fluctuations measured by CLG with a fixed continuous phase (pure octanol) flow rate of 400 μl min^{-1} and a dispersed phase (5 wt% Tween 80 aqueous solution) flow rate ranging from 0.6 μl min^{-1} to 200 μl min^{-1}, with the We number ranging from $10^{-4.36}$ to $10^{0.69}$, respectively.

inertial forces are large enough to overcome surface tension, dominating the force balance and leading to jetting flow. At a fixed continuous phase Ca value of 0.11, we used octanol and 5% Tween 80 aqueous solution as the continuous and dispersed phases, respectively, with a constant continuous phase flow rate of 400 μl min^{-1} and a variable dispersed phase flow rate ranging from 0.6 μl min^{-1} to 200 μl min^{-1}, in order to examine the dispersed phase differential pressure signals at different Weber numbers ranging from 0.0013 to 4.87. Fig. 7 shows that the results fit the expected pattern. Notably, when log We increases from negative (−0.16) to positive (0.69) values, the flow pattern changes from dripping to jetting. The results also show that dispersed phase differential pressure fluctuations diminish as We_{in} increases with measurements less than 5 Pa in jetting flow. At this point, fluctuations are within the margin of error, and distinct peaks are hard to distinguish signifying a near constant pressure differential with the onset of jetting flow. The actual transition from drop flow to jetting flow and the discreet contributions of interfacial (pressure-driven) forces and viscous (shear-driven) forces are complex topics, however, which merit a separate discussion to be addressed in future work.

Conclusions

In this study, we introduce the Capillary Laplace Gauge (CLG), a novel analysis tool which can be combined with a co-flow junction microfluidic device and an integrated image

analysis program to detect the dispersed phase differential pressure of a liquid–liquid dispersion inside a microchannel. Using the principles of the Laplace equation for a liquid–gas interface, we developed a mathematical model with reasonable physical assumptions to calculate the differential pressure from easily-measured parameters. An experimental platform constructed to realize this concept was combined with a MATLAB image analysis program to detect pressure fluctuations inside the capillary microchannels. After validation of several key assumptions in the physical model and a thorough analysis of possible device error, we discussed the differential pressure fluctuations in the context of both droplet populations and a single drop as well as the relationship between pressure fluctuation and Ca number. Finally, we examined the differential pressure data over a range of We number values when the flow regime was expected to change from drop flow to jetting flow and discussed the overall trends in differential pressure fluctuations as the We number increased. In conclusion, the CLG device described here potentially possesses unique advantages for detecting pressure in microfluidic devices including its simple, straightforward and inexpensive design, non-invasive and integrated method of visual inspection for measurement, and high sensitivity – parameters which we intend to characterize further in future work. We have demonstrated that this CLG concept can be successfully applied to study small differential changes in channel pressure throughout the droplet-breakup process in co-axial microfluidic devices. Furthermore, this CLG can potentially become a valuable tool used in various types of microfluidic devices with different geometries for conducting research involving dynamic flow and interfacial phenomena such as dynamic interfacial tension.

Acknowledgements

The authors gratefully acknowledge the support of the National Natural Science Foundation of China (21322604, 21136006, 21036002), the National Basic Research Program of China (2012CBA01203) and A Foundation for the Author of National Excellent Doctoral Dissertation of PR China (FANEDD 201053).

Notes and references

1 H. Song and R. F. Ismagilov, *J. Am. Chem. Soc.*, 2003, **125**, 14613–14619.
2 J.-H. Xu, H. Zhao, W.-J. Lan and G.-S. Luo, *Adv. Healthcare Mater.*, 2012, **1**, 106–111.
3 A. Nilghaz, D. H. B. Wicaksono, D. Gustiono, F. A. Abdul Majid, E. Supriyanto and M. R. Abdul Kadir, *Lab Chip*, 2012, **12**, 209–218.
4 A. W. Martinez, S. T. Phillips, G. M. Whitesides and E. Carrilho, *Anal. Chem.*, 2009, **82**, 3–10.
5 M. De Menech, P. Garstecki, F. Jousse and H. A. Stone, *J. Fluid Mech.*, 2008, **595**, 141–161.
6 D. R. Link, S. L. Anna, D. A. Weitz and H. A. Stone, *Phys. Rev. Lett.*, 2004, **92**, 054503.
7 M. C. Jullien, M. J. T. M. Ching, C. Cohen, L. Menetrier and P. Tabeling, *Phys. Fluids*, 2009, **21**, 072001–072006.
8 J. H. Xu, G. S. Luo, S. W. Li and G. G. Chen, *Lab Chip*, 2006, **6**, 131–136.
9 S. D. Hudson, J. T. Cabral, J. William, J. Goodrum, K. L. Beers and E. J. Amis, *Appl. Phys. Lett.*, 2005, **87**, 081905.
10 L. S. L. Wenjie, X. Jianhong and L. Guangsheng, *CIESC J.*, 2013, **64**, 476–483.
11 I. Lee, K. Park and J. Lee, *Rev. Sci. Instrum.*, 2012, **83**, 116106.
12 Y. Jin, A. Orth, E. Schonbrun and K. B. Crozier, *Opt. Express*, 2012, **20**, 24450–24464.
13 A. R. Abate, P. Mary, V. van Steijn and D. A. Weitz, *Lab Chip*, 2012, **12**, 1516.
14 P. A. Romero and A. R. Abate, *Lab Chip*, 2012, **12**, 5130–5132.
15 A. Riaud, C. Tostado, K. Wang and G. Luo, *Microfluid. Nanofluid.*, 2013, 1–10.
16 A. S. Utada, A. Fernandez-Nieves, H. A. Stone and D. A. Weitz, *Phys. Rev. Lett.*, 2007, 99.
17 T. V. Vu, S. Homma, G. Tryggvason, J. C. Wells and H. Takakura, *Int. J. Multiphase Flow*, 2013, **49**, 58–69.
18 J. H. Xu, P. F. Dong, H. Zhao, C. P. Tostado and G. S. Luo, *Langmuir*, 2012, **28**, 9250–9258.
19 J. H. Xu, S. W. Li, W. J. Lan and G. S. Luo, *Langmuir*, 2008, **24**, 11287–11292.
20 J. H. Xu, S. W. Li, C. Tostado, W. J. Lan and G. S. Luo, *Biomed. Microdevices*, 2009, 243–249.
21 L. Zhendong, L. Yangcheng, Y. Bodong and L. Guangsheng, *J. Appl. Polym. Sci.*, 2013, **127**, 628–635.
22 X. Zhao, Y. Cao, F. Ito, H. H. Chen, K. Nagai, Y. H. Zhao and Z. Z. Gu, *Angew. Chem., Int. Ed.*, 2006, **45**, 6835–6838.
23 R. D. Deegan, O. Bakajin, T. F. Dupont, G. Huber, S. R. Nagel and T. A. Witten, *Nature*, 1997, **389**, 827–829.

